

# Constraining nuclear properties in $^{94}\text{Mo}$ via a $^{93}\text{Nb}(p, \gamma)^{94}\text{Mo}$ total cross section measurement

F. Heim,<sup>\*</sup> P. Scholz, J. Mayer , M. Müller, and A. Zilges   
*University of Cologne, Institute for Nuclear Physics, 50937 Köln, Germany*



(Received 18 December 2019; accepted 28 February 2020; published 23 March 2020)

**Background:** The nucleosynthesis of the group of neutron-deficient  $p$  nuclei remains an unsolved puzzle in nuclear astrophysics. Among these nuclei,  $^{94}\text{Mo}$  is one of the most abundant and is notoriously underproduced in theoretical network calculations. In these networks, the respective cross sections and reaction rates play a crucial role. Since many reactions of astrophysical relevance are not accessible in the laboratory, a global and robust theoretical framework is required to provide reliable predictions.

**Purpose:** Extending the experimental database on the one hand and direct or indirect studies of the respective nuclear physics properties on the other hand are the key tasks of experimental nuclear astrophysics. For this purpose, total cross sections of the  $^{93}\text{Nb}(p, \gamma)^{94}\text{Mo}$  reaction have been measured at proton energies between 2.0 and 5.0 MeV.

**Methods:** In-beam  $\gamma$ -ray spectroscopy has been utilized to measure total cross sections. In general, the total cross sections depend strongly on the  $\gamma$ -ray decay widths in  $^{94}\text{Mo}$ , which are derived from the  $\gamma$ -ray strength function and the nuclear level density. In our analysis we use a Bayesian optimization analysis to disentangle the effects of the  $\gamma$ -ray strength function and the nuclear level density in  $^{94}\text{Mo}$ .

**Results:** The total cross-section results reveal a significant discrepancy with respect to formerly published values. We propose parametrizations for the nuclear level density in  $^{94}\text{Mo}$  based on the microscopic level densities from Hartree-Fock-Bogoliubov calculations. Moreover, we present  $\gamma$ -ray strength functions for the  $E1$  and  $M1$  mode in  $^{94}\text{Mo}$  that reveal a low-energy enhancement for  $M1$  radiation and agree nicely with previous results.

**Conclusions:** A model-independent approach to study  $E1$  and  $M1$  strength functions has been presented. In general, radiative capture cross sections are a well-suited tool to constrain the reaction rates in reaction networks but also provide insight into the statistical  $\gamma$ -decay behavior of atomic nuclei.

DOI: [10.1103/PhysRevC.101.035807](https://doi.org/10.1103/PhysRevC.101.035807)

## I. INTRODUCTION

The details of the processes that are responsible for the nucleosynthesis of heavy nuclei are still not completely understood. The neutron capture processes produce a large fraction of the heavy elements [1–4] but bypass a group of 30 to 35 stable, proton-rich nuclei ranging from  $^{74}\text{Se}$  to  $^{196}\text{Hg}$ . The different mechanisms that trigger the nucleosynthesis of these  $p$  nuclei are gathered under the umbrella term of  $p$  processes. Detailed information can be found, e.g., in Refs. [5–7].

One of the first quantitative calculations of  $p$ -process yields from a type-II supernova (SNII) explosion found a significant underproduction of the light  $p$  nuclei  $^{92,94}\text{Mo}$  and  $^{96,98}\text{Ru}$  [8] and were confirmed later, see e.g. [9]. Various solutions for this problem have been proposed which are either related to the uncertainty of the explicit astrophysical scenario and site [5,6,10] or to uncertainties in the nuclear physics parameters used for calculating the respective reaction rates. Some years ago, the  $\nu p$  process has been introduced [11] which aimed at solving the underproduction problem: strong neutrino flows acting on the hot proton-rich matter of core-collapse supernovae induce the  $\bar{\nu}_e + p \rightarrow n + e^+$  reaction producing free neutrons which then induce  $(n, p)$  reactions

on proton-rich nuclei. Thus, matter is driven back towards the valley of stability and the production of the light  $p$  isotopes should be enhanced. However, radionuclide studies of  $^{92}\text{Nb}$  found in meteorites have put constraints on the role of the  $rp$  and  $\nu p$  processes in the nucleosynthesis of Mo and Ru  $p$  isotopes. It turned out that a significant contribution is unlikely in supernova type-II scenarios [6,12]. Additionally,  $p$ -process contributions have been found in type-Ia supernova, which do not suffer from this severe underproduction [13], but a more thorough analysis of the role of type-Ia supernova in the solar composition of  $p$  nuclei is needed [14,15].

From the experimental nuclear physics point of view, high uncertainties are expected from the photodisintegration rates which are acting in the complex  $\gamma$  process network [6,8,9], as well as from the neutron- and proton-capture rates. For most of the reaction rates that are involved in this network, detailed experimental information is neither available nor accessible in the laboratory. Hence, in many cases, one has to rely completely on theoretical models. In particular, cross sections and reaction rates need to be extrapolated to astrophysical energies, i.e., far below the Coulomb barrier, by using theoretical calculations [16,17]. Therefore, it is essential to test the calculated cross sections in experiments and to provide more robust input to the network calculations and increase their predictive power.

<sup>\*</sup>fheim@ikp.uni-koeln.de

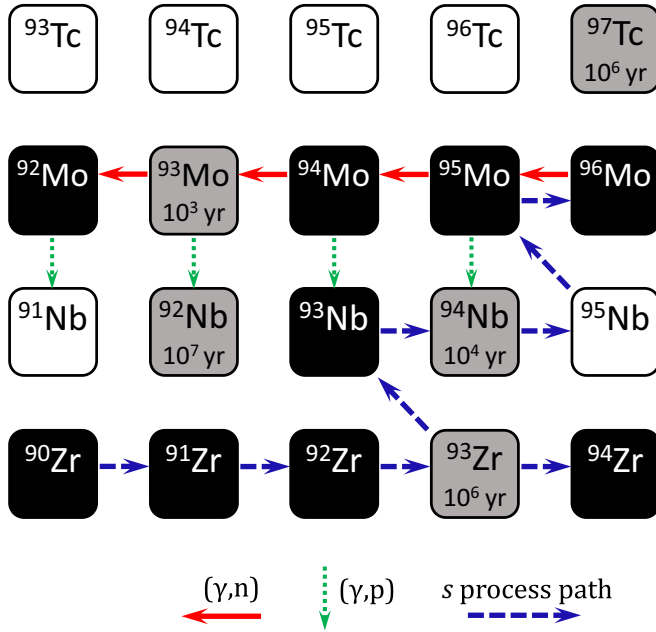


FIG. 1. Reaction path for the  $\gamma$  process in the molybdenum isotopes. A series of  $(\gamma, n)$  reactions acting on stable  $s$ -process seed nuclei drive the path towards the neutron-deficient region. At nuclei with competing  $(\gamma, n)$  and  $(\gamma, p)$  or  $(\gamma, \alpha)$  cross sections, a branching into a neighboring isotopic chain is possible.

Theoretical cross sections and reaction rates are usually obtained using the Hauser-Feshbach statistical model [18,19], whose uncertainties are mainly affected by the nuclear physics input parameters such as  $\gamma$ -ray strength functions ( $\gamma$ -SF), nuclear level densities (NLDs), and particle + nucleus optical-model potentials (OMPs) [5,20]. At low energies, radiative capture cross sections are usually very sensitive to the  $\gamma$  width which is composed of the  $\gamma$ -ray strength function and nuclear level densities [5,6,20]. In the past, it was found that the established proton and neutron optical-model potentials provide very accurate results, whereas the available  $\alpha$ -OMPs can easily yield discrepancies between experimental and calculated cross sections of a factor of three or even more (see Refs. [21–26] and references therein).

Although numerous reactions are involved in the  $\gamma$ -process network, only a few have a significant relevance to the determination of the reaction paths. Thus, sensitivity studies to identify these key reactions have been carried out [27,28]. One key reaction is  $^{94}\text{Mo}(\gamma, p)^{93}\text{Nb}$  which might compete with the respective  $(\gamma, n)$  reaction and affects the overall abundance of  $^{94}\text{Mo}$  (see Fig. 1). To account for the thermal population of excited states in the stellar plasma, it is more useful to measure the inverse reaction, i.e., the radiative capture. Hence, the aim of this work is to measure the  $^{93}\text{Nb}(p, \gamma)^{94}\text{Mo}$  cross section, which was experimentally addressed some time ago in Ref. [29].

The analysis of the  $^{93}\text{Nb}(p, \gamma)^{94}\text{Mo}$  reaction has been carried out by means of high-resolution in-beam  $\gamma$ -ray spectroscopy. This method has been described, e.g., in Refs. [24,30–35], and is not limited to reactions with unstable reaction products as is the case for the activation method (see,

e.g., Ref. [36]). The total  $(p, \gamma)$  cross-section values (in the following called total cross section) are mainly sensitive to the NLD and  $\gamma$ -SF in  $^{94}\text{Mo}$ , and we present an approach that disentangles these two properties. Finally, we propose NLD and  $\gamma$ -SF data for  $^{94}\text{Mo}$  and compare them to results obtained by different techniques. This paper is structured as follows: In Sec. II a brief summary of the experimental setup and method is given, followed by an overview of the data analysis in Sec. III. In Sec. IV our experimental results are presented and an approach is given for the statistical model analysis using TALYS [37].

## II. EXPERIMENTAL SETUP AND METHOD

The  $^{93}\text{Nb}(p, \gamma)^{94}\text{Mo}$  experiment has been performed at the 10 MV FN-Tandem accelerator at the Institute for Nuclear Physics at the University of Cologne. The target chamber, which is dedicated to nuclear astrophysics experiments, was mounted within the HORUS  $\gamma$ -ray spectrometer [35]. HORUS consists of up to 14 HPGe detectors which can be partly equipped with bismuth germanate (BGO) shields. The target chamber has been renewed recently and allows us to place the detectors at very close distances of about 9 cm to the target, which significantly increases the total detection efficiency [35]. The beam current is read out at the target, the chamber, and a Faraday cup behind the target. A suppression voltage of  $-400$  V is applied to prevent  $\delta$  electrons from escaping the chamber. The target can be monitored by using a built-in silicon detector placed at an angle of  $135^\circ$ .

After the bombardment of the  $^{93}\text{Nb}$  target nuclei with protons of energy  $E_p$ , a highly excited compound nucleus is formed with an excitation energy of  $E_x = Q + E_{\text{c.m.}}$ . The  $Q$  value of the  $^{93}\text{Nb}(p, \gamma)^{94}\text{Mo}$  reaction is  $+8490$  keV. Figure 2 shows a schematic illustration of the reaction and the subsequent  $\gamma$  decays in  $^{94}\text{Mo}$ . *Total cross sections* can be derived from measuring all  $\gamma$ -ray transitions into the ground state of  $^{94}\text{Mo}$ . Using high-resolution in-beam  $\gamma$ -ray spectroscopy, the prompt  $\gamma$ -ray decay into different discrete states in  $^{94}\text{Mo}$  can also be observed and partial cross sections can be derived.

### Beam and target characteristics

The astrophysically relevant Gamow window for the  $^{93}\text{Nb}(p, \gamma)^{94}\text{Mo}$  reaction lies between 1.7 and 3.4 MeV at  $T = 3.0$  GK. In this study, proton beam energies between 2.0 and 5.0 MeV have been chosen. The beam energy was determined precisely using the prompt  $\gamma$ -ray decay of the excited compound nucleus.

A mono-isotopic, metallic  $^{93}\text{Nb}$  target of  $1.1$  mg/cm<sup>2</sup> thickness has been used and irradiated at proton beam intensities between 500 and 900 nA for 0.5 to 8 hours. For the beam energies of  $E_p = 3.0$  MeV and  $E_p = 3.5$  MeV measurement times of 87 hours and 133 hours, respectively, have been chosen. Those long-term measurements aimed at observing the prompt  $\gamma$  decay of the excited compound nucleus, for which very low cross sections in the nb region were expected.

The target thickness was determined using Rutherford Backscattering Spectrometry (RBS) at the RUBION facility in Bochum, Germany before and after the experiment as well

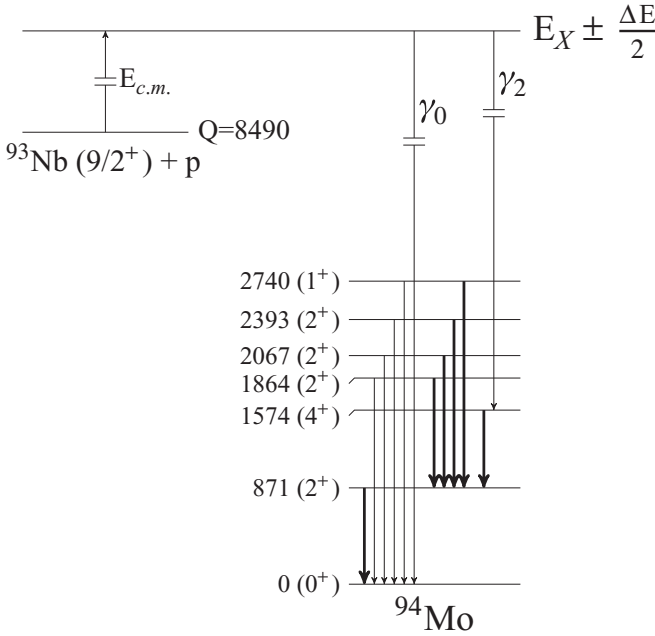


FIG. 2. Illustration of the reaction mechanism that leads to the highly excited compound nucleus after a radiative-capture reaction. The compound state contains numerous unresolvable resonances and has a width of  $\frac{\Delta E}{2}$ , where  $\Delta E$  denotes the energy loss. It then deexcites either directly into the ground state of  $^{94}\text{Mo}$  ( $\gamma_0$ ) or into other low-lying levels via different  $\gamma$ -ray cascades. Only states which can deexcite at least partly into the ground state are shown. The dominant branchings are shown by thick arrows. All data were taken from Ref. [38].

as during the experiment using the RBS detector mounted at the target chamber in Cologne [35,39]. A 200 mg/cm<sup>2</sup> thick gold foil was attached to the backside of the targets to stop the beam. The energy loss inside the target is calculated via SRIM [40], resulting in an average energy loss  $\Delta E$  between 44 and 81 keV. The effective interaction energy of the protons is defined as

$$E_{\text{eff}} = E_p - \frac{\Delta E}{2}, \quad (1)$$

where  $E_p$  denotes the beam energy of the impinging protons.

### III. DATA ANALYSIS

#### A. Angular correlations

The absolute cross section is given by

$$\sigma(p, \gamma)_{\text{tot}} = \frac{N_{(p,\gamma)}}{N_p N_T}, \quad (2)$$

where  $N_p$  and  $N_T$  are the number of projectiles and target nuclei per area, respectively, and  $N_{(p,\gamma)}$  is the number of proton-capture reactions which is derived from the  $\gamma$ -ray spectra. After creation of the excited compound nucleus, each emitted  $\gamma$ -ray follows an angular distribution  $W(\Theta)$  with respect to the beam axis. The experimental yield  $Y(E_\gamma)$  is corrected for the full-energy peak efficiency  $\epsilon(E_\gamma)$  and the

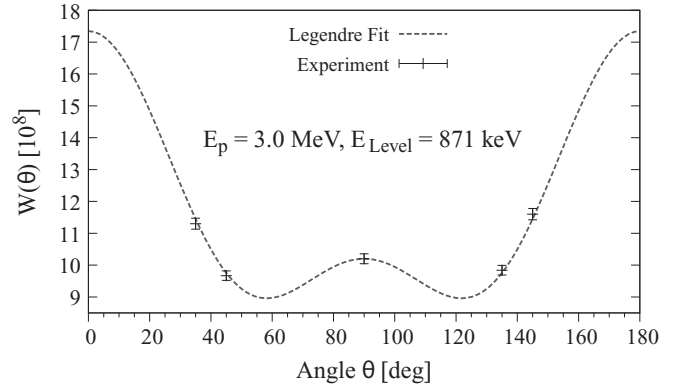


FIG. 3. The emitted  $\gamma$  rays from the compound nucleus follow an angular correlation. The  $\gamma$ -ray intensities are measured at five individual angles and fit by a series of Legendre polynomials. This picture shows the  $2_1^+ \rightarrow$  g.s. transition in  $^{94}\text{Mo}$  with  $E_\gamma = 871$  keV for a proton beam energy of 3.0 MeV. For the measured data points only the statistical error is shown.

dead time correction of the data acquisition  $\tau$ :

$$W(\Theta) = \frac{Y(E_\gamma)}{\epsilon(E_\gamma)\tau}. \quad (3)$$

The angular distribution is obtained by fitting a sum of Legendre polynomials to the experimental values:

$$W(\Theta) = A_0 \left( 1 + \sum_{k=2,4} \alpha_k P_k(\cos \Theta) \right). \quad (4)$$

These angular distributions are obtained for each  $\gamma$ -ray transition at each beam energy and the sum of all  $A_0$  coefficients represents the total number of proton captures,  $N_{(p,\gamma)}$  [35]. As an example, Fig. 3 shows the measured intensities of the  $2_1^+ \rightarrow$  g.s. transition in  $^{94}\text{Mo}$  at five different angles along with the fitted Legendre polynomials.

#### B. $\gamma$ -ray spectra

The experimental yield  $Y(E_\gamma)$  of the  $^{93}\text{Nb}(p, \gamma)^{94}\text{Mo}$  reaction is obtained from the peak volume of all ground-state transitions that are observed in the  $\gamma$ -ray spectra. Figure 4 shows parts of a typical  $\gamma$ -ray spectrum for beam energies  $E_p = 2$  MeV and  $E_p = 5$  MeV. The beam-on-target times were 2 hours and 30 minutes, respectively.  $^{93}\text{Nb}$  has no isotopic neighbors, so the  $^{93}\text{Nb}(p, n)^{93}\text{Mo}$  reaction is the only competing reaction. At lower beam energies the  $(p, n)$  contribution is almost negligible and clean spectra showing only  $\gamma$ -ray transitions in  $^{94}\text{Mo}$  were obtained (see the inset of Fig. 4). Other transitions stem from reactions in the  $^{197}\text{Au}$  stopper foil or on  $^{65}\text{Cu}$  (the material of the cooling finger, which surrounds the target). Due to the low beam energy, the corresponding reaction cross sections are very small and even  $^{40}\text{K}$  background radiation is observable. At higher beam energies, the  $(p, n)$  reaction is the dominating reaction mechanism and the obtained  $\gamma$ -ray spectra are contaminated by numerous transitions in  $^{93}\text{Mo}$ .

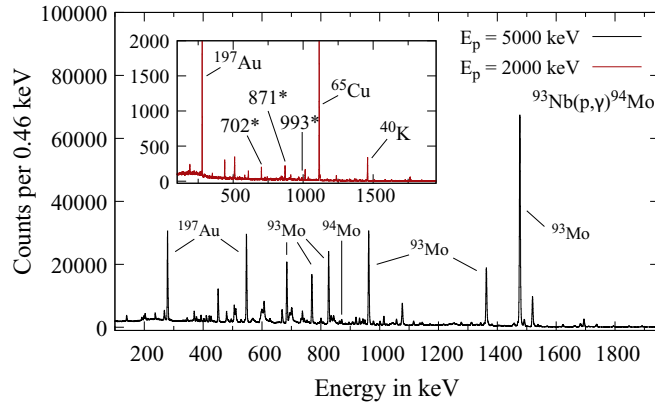


FIG. 4. Excerpt from a spectrum of the  $^{93}\text{Nb}(p, \gamma)^{94}\text{Mo}$  reaction for one HPGe detector with BGO shield. The black spectrum shows the  $\gamma$ -ray spectrum for a proton beam of  $E_p = 5$  MeV (irradiated for 30 minutes) and the red spectrum for  $E_p = 2$  MeV (irradiated for 2 hours). Transitions from the reaction of interest are marked with an asterisk. At lower beam energies the produced activity was very low and background radiation from  $^{40}\text{K}$  could be observed. At higher beam energies most observed transitions stem from the  $^{93}\text{Nb}(p, n)^{93}\text{Mo}$  reaction.

For the determination of total cross sections the peak volumes of all ground-state (g.s.) transitions have to be determined. In the present case, it turned out that it is sufficient to measure the intensity of the  $2_1^+ \rightarrow \text{g.s.}$  transition with  $E_\gamma = 871$  keV in  $^{94}\text{Mo}$ . This can be directly derived from the level scheme shown in Fig. 2. It shows the first seven low-lying states in  $^{94}\text{Mo}$  and the strength of their decay branchings is indicated by the thickness of the arrows. Apparently, all states that can decay into the g.s. exhibit a dominating  $\gamma$ -decay branching of at least 85% into the  $2_1^+$  state at  $E_\gamma = 871$  keV. Hence, one can expect that by far the largest contribution to the total g.s. population can be attributed to the  $2_1^+ \rightarrow \text{g.s.}$  transition. This assumption was strengthened experimentally, since barely any significant intensity from other g.s. transitions in the  $\gamma$ -ray spectra could be found.

Additionally, we verified our arguments using the long-term measurements of the  $^{93}\text{Nb}(p, \gamma)^{94}\text{Mo}$  reaction at  $E_p = 3.0$  MeV and  $E_p = 3.5$  MeV. In those cases, small traces of other g.s. transitions apart from the  $2_1^+ \rightarrow \text{g.s.}$  transition were observed and their contribution to the g.s. population was calculated. Figure 5 shows the different contributions derived from these long-term measurements. It proves that nearly all g.s. population proceeds via the  $2_1^+$  state at  $E_\gamma = 871$  keV. The impact of other g.s. transitions amounts to less than 7%. We showed in Ref. [39] that these relations do not vary significantly with the beam energy. Consequently, for all other beam energies only the peak volume of the  $E_\gamma = 871$  keV transition was taken into account and was corrected for missing g.s. transitions by an average factor of 1.05(2). Because the  $2_1^+$  state at  $E_\gamma = 871$  keV is fed by numerous higher lying states, the effect of angular correlations is quite small (see Fig. 3). Note that no prompt  $\gamma$  decay from the excited compound nucleus into the g.s. was observed, which is

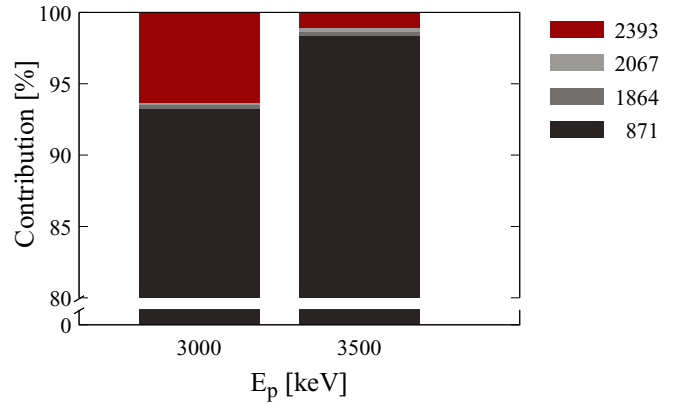


FIG. 5. Contributions to the ground-state population from different excited states of the  $^{93}\text{Nb}(p, \gamma)^{94}\text{Mo}$  reaction at the two beam energies  $E_p = 3.0$  MeV and  $E_p = 3.5$  MeV. Note that the  $y$  scale is discontinuous. About 95% of the g.s. population stems from the  $2_1^+ \rightarrow \text{g.s.}$  transition at  $E_\gamma = 871$  keV. As shown in an earlier work, these ratios do not tend to vary with beam energy significantly [39].

to be expected. The  $^{93}\text{Nb}$  target nucleus has  $J_0^\pi = 9/2^+$ . After the proton capture, predominantly  $4^+$ ,  $5^+$ ,  $4^-$ , and  $5^-$  states are populated, which requires emitting  $\gamma$  rays that carry an angular momentum of at least four to decay directly to the ground state. This is very unlikely and a  $\gamma$ -ray decay into higher-spin states is favored.

The experimental yields from the  $\gamma$ -ray spectra need to be corrected for the full-energy peak efficiencies of the detectors. Therefore, a  $^{226}\text{Ra}$  standard calibration source was used for the low-energy efficiency calibration. For absolute  $\gamma$ -ray detection efficiencies of  $\gamma$ -ray energies up to 5 MeV, in-house-produced  $^{56}\text{Co}$  and  $^{66}\text{Ga}$  sources have been used. These sources have relatively short half-lives of 77 days and 9.5 hours, respectively, but emit numerous  $\gamma$  rays up to an energy of  $E_\gamma = 4.8$  MeV [41,42]. The total detection efficiency of the HORUS array amounts to about 3% at  $E_\gamma = 1.3$  MeV in the configuration used for this experiment.

The digital data acquisition at the HORUS  $\gamma$ -ray spectrometer stores all events in an event-by-event listmode format. Hence, in addition to single spectra  $\gamma\gamma$ -coincidence matrices can be generated offline, which is a very powerful tool to suppress beam-induced background [35]. The  $\gamma\gamma$ -coincidence technique allows us to assign  $\gamma$ -ray transitions easily to a certain nucleus and to approximate the intensity of transitions which might be buried in the Compton background of higher-energy  $\gamma$ -ray transitions. In the present case, the  $\gamma\gamma$ -coincidence method was applied to determine unambiguously the 871 keV yield. A  $0^+$  state at  $E_\gamma = 1742$  keV in  $^{94}\text{Mo}$  is reported in the literature [38] which could deexcite via another 871 keV  $\gamma$ -ray into the  $2_1^+$  state at  $E_\gamma = 871$  keV. It is shown in Ref. [35] that its impact can be neglected.

Recently,  $\gamma\gamma$  matrices have been used to construct discrete two-step  $\gamma$ -ray cascade spectra [43–46]. In Cologne, this technique has been utilized to determine the intensity of prompt  $\gamma$ -ray transitions from the excited compound nucleus which yield major information about the  $\gamma$ -ray strength function. Details can be found in Ref. [47].

TABLE I. Total cross-section values  $\sigma_{\text{tot}}$  for the  $^{93}\text{Nb}(p, \gamma)^{94}\text{Mo}$  reaction as a function of center-of-mass energy. For the beam energies of  $E_p = 3.0$  MeV and  $E_p = 3.5$  MeV four g.s. transitions have been observed in addition to the  $2_1^+ \rightarrow$  g.s. transition. For all other beam energies, only the intensity of the  $2_1^+ \rightarrow$  g.s. transition with  $E_\gamma = 871$  keV has been used and corrected by a factor of 1.05(2). See text for details.

$E_{c.m.}$ [keV]	$\sigma_{\text{tot}}$ [ $\mu\text{b}$ ]
$1959 \pm 23$	$3.48 \pm 0.51$
$2162 \pm 23$	$10.7 \pm 1.5$
$2465 \pm 22$	$39.8 \pm 5.7$
$2767 \pm 22$	$75 \pm 11$
$2969 \pm 22$	$116 \pm 13$
$3069 \pm 22$	$148 \pm 21$
$3371 \pm 22$	$219 \pm 32$
$3472 \pm 22$	$227 \pm 26$
$3673 \pm 21$	$188 \pm 27$
$3975 \pm 21$	$132 \pm 19$
$4476 \pm 21$	$177 \pm 23$
$4978 \pm 21$	$335 \pm 48$

## IV. RESULTS AND ANALYSIS

### A. Total cross-section results

The total cross-section values obtained in this work are listed in Table I. Energies are given as effective proton energies corrected for the energy loss. The uncertainties in the cross-section values are composed of the uncertainties in the number of projectiles ( $\approx 5\%$ ), the target thickness ( $\approx 10\%$ ), full-energy peak efficiency ( $\approx 8\%$ ), and the statistical error after fitting the Legendre polynomials ( $\approx 3\%$ ).

The only other experimental data reporting on this reaction are from Ref. [29]. Figure 6 shows these older results along with the new results obtained in this work. In particular at

energies above about 3.0 MeV significant discrepancies are found. The systematic deviations from our values by a factor of about 1.4 might be explained by various experimental error sources: In Ref. [29] no suppression voltage is mentioned. Only the 871 keV g.s. transition is taken into account. Further discrepancies might arise from using the same angular distribution for all beam energies above 3.0 MeV.

The experimental results for the total cross sections obtained in this work are compared with TALYS v1.9 [37] calculations based on different models of nuclear physics input parameters which shall be introduced now.

### B. Statistical model analysis

The precision of calculated cross sections using a Hauser-Feshbach code like TALYS is mainly governed by the models chosen for the nuclear physics input parameters. In the case of  $(p, \gamma)$  reactions, the most important parameters are the nuclear level density (NLD),  $\gamma$ -ray strength function ( $\gamma$ -SF), and particle + nucleus OMPs. The proton and neutron OMP has been investigated intensively during the last decades and global models such as the Koning and Delaroche OMP [49] have proven their reliability and robustness. Since this model also agrees satisfyingly well with the  $(p, n)$  cross sections on  $^{93}\text{Nb}$  [50] (which is almost exclusively sensitive to the proton OMP [51]), we have chosen this model for our calculations. We will focus on the impact of NLD and  $\gamma$ -SF in the following. However, in contrast to the simple concept of comparing theoretical results using all available models for NLD and  $\gamma$ -SF to experimental values, we will follow a more strategical approach. The idea is as follows: We start with an investigation of various NLD models and their predictions on the cumulative number of levels. Via the comparison to experimentally determined level densities, a suitable model for the NLD is proposed. Subsequently, the remaining discrepancies between theoretical and experimental cross sections are mainly affected by the  $\gamma$ -SF.

### C. Level density studies

The main task of theoretical NLD models is to provide the number of levels at a certain excitation energy and the corresponding spin-parity distribution, see, e.g., Ref. [52] for details. In the last years microscopic NLD models based on a combinatorial approach have shown their predictive power [48] and, by now, they can be tuned to the same level of accuracy as phenomenological models such as the back-shifted Fermi gas model [53] or the Gilbert-Cameron model [54]. Moreover, the spin and parity distributions are based on a more realistic combinatorial approach [55]. In many cases, the equal-parity assumption is not valid and this feature affects the calculations, see, e.g., Ref. [45]. In the case of  $^{94}\text{Mo}$  we have chosen to start our analysis with the microscopic level density based on Hartree-Fock-Bogoliubov (HFB) calculations and the Skyrme interaction [48]. In TALYS 1.9 this is implemented as *ldmodel 5*.

The tabulated, microscopic level-density values  $\rho_{\text{tab}}$  are composed of the level densities for positive and negative parity and can be adjusted within the TALYS code via the

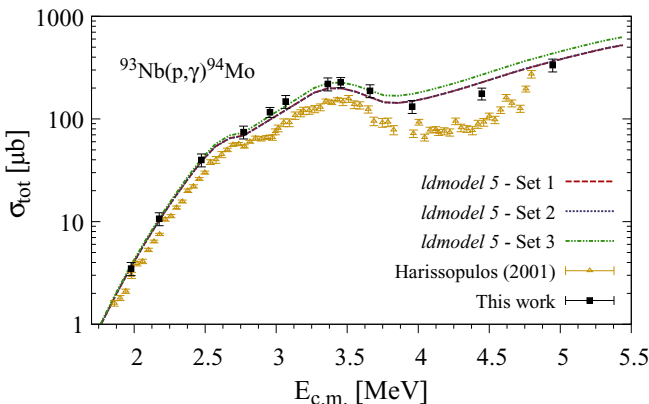


FIG. 6. Total  $^{93}\text{Nb}(p, \gamma)^{94}\text{Mo}$  cross sections obtained in this work (black squares). Above proton energies of about 3 MeV, the new results are systematically higher than the results reported in Ref. [29] (yellow triangles). Statistical model calculations using the TALYS 1.9 code [37] and the microscopic level densities from Hilaire's combinatorial tables [48] are in good agreement with the new values. See Sec. IV C for details.

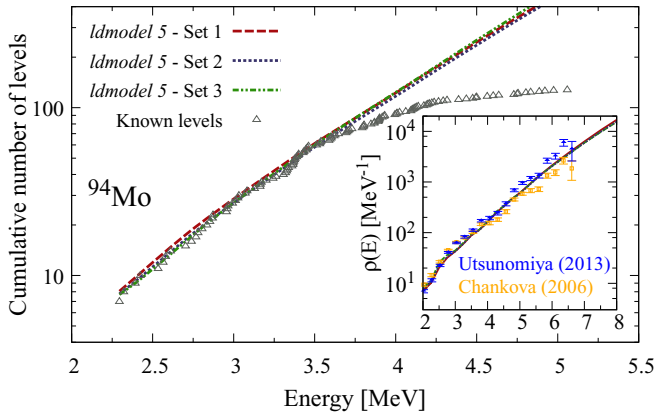


FIG. 7. Cumulative number of levels in  $^{94}\text{Mo}$ . Previously experimentally known levels are marked with triangles [38]. The predicted number of levels for three different parameter sets of the microscopic NLD from Ref. [48] are in very good agreement with the low-lying experimental region. The inset shows the calculated level densities in the high-energy region compared with results from Oslo-type experiments [56,57].

following parametrization:

$$\rho(E_x, J, \pi) = e^{c\sqrt{E_x - \delta}} \rho_{\text{tab}}(E_x - \delta, J, \pi), \quad (5)$$

where by default the scaling parameter  $c = 0$  and the “pairing shift”  $\delta$  gives the opportunity to obtain the level density at a different energy, i.e. to shift the NLD. We mention that the existence of this scaling option does not put the microscopic models on the level of phenomenological ones. Usually, these parameters need to be adjusted to fit experimental results [17,48].

In our studies we varied both scaling parameters systematically in order to achieve the best agreement with the low-lying level scheme up to energies of 3.5 MeV. Above this value the experimentally known levels are quite scarce. Figure 7 shows the number of levels predicted by the microscopic NLD model along with predictions using three different parameter sets. Set 1 ( $c = -0.45$ ,  $\delta = 0.6$ ) denotes the model that gave the best reproduction of the total cross-section values and set 3 ( $c = -0.31$ ,  $\delta = 0.76$ ) provides the best agreement with the cumulative number of levels. Set 2 ( $c = -0.42$ ,  $\delta = 0.67$ ) yielded the best combined agreement. However, the differences are small and it turned out that slightly different combinations of parameters yield very similar predictions. Subsequently, we compared the proposed parametrizations to level densities deduced experimentally by means of the Oslo technique [56,57]. The agreement is very good (see the inset of Fig. 7).

The calculated cross sections using the TALYS 1.9 code that are shown in Fig. 6 imply these NLD parametrizations, respectively, along with the microscopic Gogny D1M + QRPA model for the  $\gamma$ -SF [58]. This model has been chosen because it showed convincing results in recent studies, see, e.g., Refs. [57,59]. Moreover, this combination of NLD and  $\gamma$ -SF is the most self-consistent combination since both models are based on the same HFB model.

#### D. $E1$ and $M1$ strength-function studies

The investigation of  $\gamma$ -ray strength functions has been addressed for several decades. At present, there is no experimental method that provides a full picture of the  $\gamma$ -SF over a wide energy range. Several structures caused by collective phenomena within the atomic nucleus have been observed in the past years: At low energies an unexpected enhancement (“up-bend”) was found in several medium-mass nuclei. The origin of this enhancement and in particular its radiation type is the subject of current research [60–64]. At energies around the neutron separation energy, an  $E1$  pygmy dipole resonance was found in several nuclei [65]. Both phenomena can significantly affect the reaction rates relevant for nuclear astrophysics [66,67]. For details on the origin of various models that are available for the  $\gamma$ -SF, we refer to Ref. [68].

The remaining deviations between TALYS calculations and experimental cross sections noticeable in Fig. 6 are most likely governed by uncertainties in the  $\gamma$ -SF, in detail the  $E1$  and  $M1$  strength in  $^{94}\text{Mo}$ . First, we investigated the sensitivity of the total ( $p, \gamma$ ) cross section on modifications of the  $E1$  and  $M1$  strength function in various energy regions. It turned out that the results are mainly affected by the strength at  $\gamma$ -ray energies between 1 and 8 MeV. Moreover, we want to find the explicit shapes of the  $E1$  and  $M1$  strength functions that minimize the deviations between calculated and experimental cross sections. Therefore, we calculated iteratively numerous input strength functions by means of a Bayesian hyperparameter-optimization algorithm within the aforementioned energy range [69]. Subsequently, for each input strength function, total cross sections have been calculated with TALYS. For both  $E1$  and  $M1$  strength, a modified Lorentzian has been used, similar to Ref. [45]:

$$f(E_\gamma) = 8.68 \times 10^{-8} \text{ (mb}^{-1} \text{ MeV}^{-2}\text{)} \\ \times C_{M1} \left[ \frac{\sigma E_\gamma \Gamma^2}{(E_\gamma^2 - E_R^2)^2 + E_\gamma^2 \Gamma^2} + A e^{(-BE_\gamma)} \right] e^{C(E_\gamma - E_X)}. \quad (6)$$

A possible low-energy enhancement is emulated by an additional exponential function. The alteration of the general slope of the Lorentzian is allowed by a term  $e^{C(E_\gamma - E_X)}$ , where  $E_X = 12.3$  MeV has been chosen as the average excitation energy of the compound nucleus. Other values have been tested, but gave no significant variations. The  $M1$  scaling parameter  $C_{M1}$  has been applied to all calculated  $M1$  strength functions and accounts for the systematic experimental observations of the  $f_{M1}/f_{E1}$  ratio which varies between 0.1 and 0.7 [68]. The GDR values for  $E1$  and  $M1$  have been taken from Ref. [68] as well. It has been tested that the strength functions described by Eq. (6) are able to mimic all currently known prescriptions of  $\gamma$ -ray strength functions [45]. We apply the tree-structured Parzen estimator (TPE) approach for an optimization of the hyperparameters A, B, C, and  $C_{M1}$ . This algorithm searches for the optimal hyperparameter configuration based on the current model and already available information. Finally, all combinations of  $E1$  and  $M1$  strength functions are selected that reproduce the total  $^{93}\text{Nb}(p, \gamma)^{94}\text{Mo}$  cross

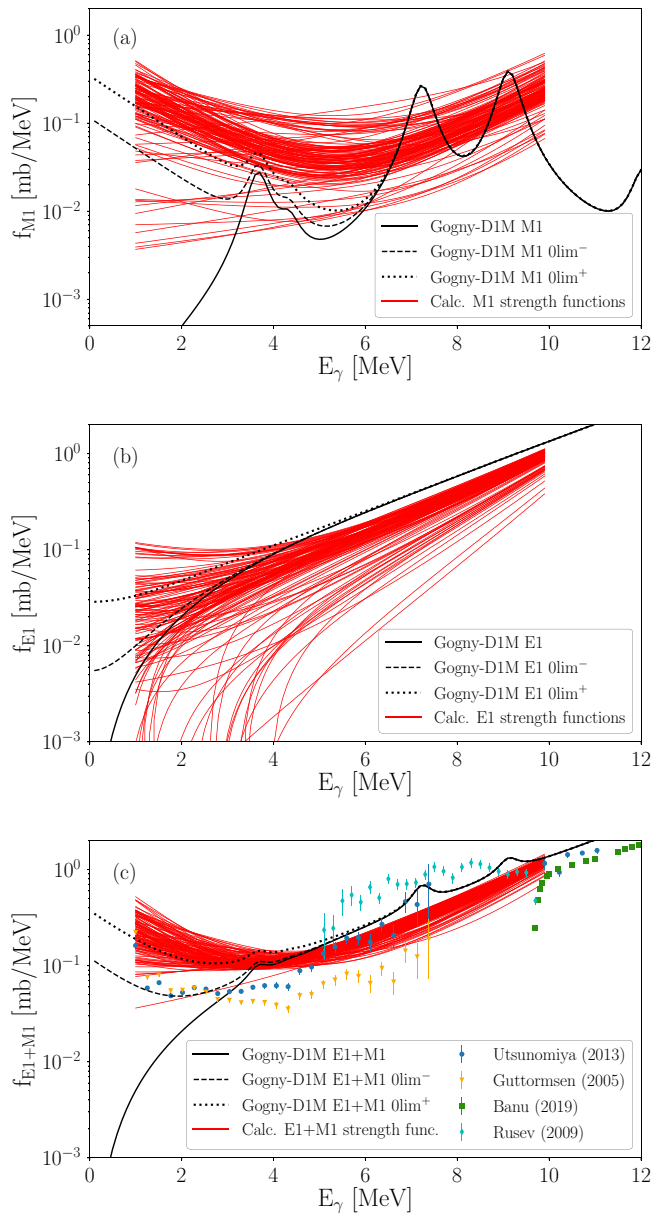


FIG. 8. Panels (a)–(c) show the calculated  $M1$ ,  $E1$ , and  $E1 + M1$  strength functions for  $^{94}\text{Mo}$ , respectively. The red lines show all strength functions that reproduce the  $^{93}\text{Nb}(p, \gamma)^{94}\text{Mo}$  cross section within a 95% confidence interval. The simulated strength functions are compared with the Gogny nucleon-nucleon interaction-based D1M + QRPA model [58] and the D1M + QRPA + 0lim extension [70]. In addition, panel (c) shows experimental strength-function data deduced via Oslo-type experiments [57,61], as well as photonuclear [71] and photoabsorption data [72].

sections within a 95% confidence interval. Figure 8 shows the selected  $E1$ ,  $M1$ , and  $E1 + M1$  strength functions along with predictions from the Gogny D1M + QRPA model [58] as well as the D1M + QRPA + 0lim description [70]. The latter one represents an extension of the D1M + QRPA absorption strength functions to the deexcitation strength function. In particular, it provides an insight in the low-energy limit of the strength functions and accounts for the low-energy

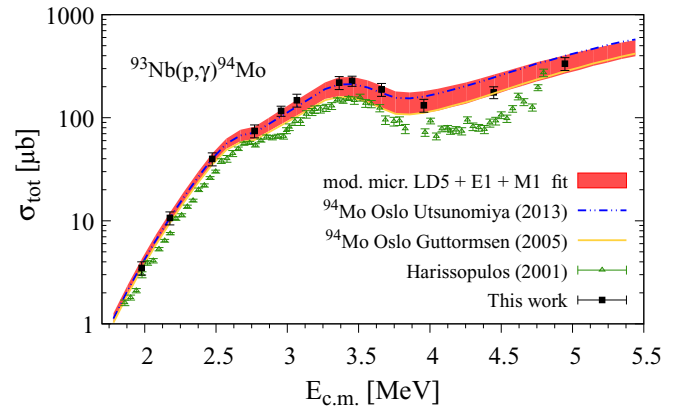


FIG. 9. Same as Fig. 6, but the TALYS calculations using all selected shapes for  $E1$  and  $M1$  strength from Fig. 8 are shown as red-shaded area. In addition, calculated cross sections using NLD and  $\gamma$ -SF data deduced via the Oslo technique are plotted [56,57,61]. See text for details.

enhancement which was observed in many  $M1$  shell-model calculations (see, e.g., Refs. [73–75]) or, as mentioned above, in several experiments.

Although there are large variations in the slope of the calculated strength functions, one can clearly see that the vast majority of  $M1$  strength functions tend to exhibit a low-energy enhancement. This trend is nicely reproduced by the zero-limit extension of the D1M + QRPA calculations, for which a lower and an upper limit is provided. Note that this low-energy enhancement is not predefined by the model given in Eq. (6) but all shapes for the  $M1$  strength function are possible and equally probable. The observed up-bend for the  $M1$  strength seems to be necessary to describe the total cross sections adequately. For the  $E1$  strength no clear trend towards the low-energy region can be identified, although a constant or decreasing trend is most likely favored below  $E_\gamma \approx 4$  MeV. For energies above 4 MeV, all calculated  $E1$  functions indicate that the Gogny-D1M + QRPA calculations are too high by at least  $\approx 20\%$ . The sum of  $E1$  and  $M1$  functions shows significantly less variations and the low-energy up-bend is clearly pronounced. The calculated functions are in good agreement with the predictions of the zero-limit D1M + QRPA model below  $E_\gamma \approx 4$  MeV and reproduce the experimental observations in  $^{94}\text{Mo}$  deduced via the Oslo technique [57,61] above  $E_\gamma \approx 5$  MeV. Above the neutron separation energy of  $S_n = 9.7$  MeV photoabsorption data from  $(\gamma, n)$  experiments are available [57,71]. For better visibility we have drawn all strength functions up to  $E_\gamma = 10$  MeV, which show a fairly good agreement with the previous measurements. From the current investigations, the low-energy enhancement can be assigned to the  $M1$  mode. The final calculated cross sections using all selected  $E1$  and  $M1$  strength functions are shown in Fig. 9. We also plotted the calculated cross sections using NLD and  $\gamma$ -SF obtained from Oslo-type experiments as input [56,57,61].

To illustrate the astrophysical importance of the nuclear physics models constrained experimentally in this work, the stellar reaction rate of the  $^{94}\text{Mo}(\gamma, p)$  and  $^{94}\text{Mo}(\gamma, n)$

TABLE II. Ratio of stellar reaction rates for  $(\gamma, p)/(\gamma, n)$  on  $^{94}\text{Mo}$  for typical  $p$ -process temperatures given in  $\text{cm}^3 \text{s}^{-1} \text{mol}^{-1}$ . The rates were calculated by using the  $\gamma$ -SF and NLD obtained in this work (this work). In addition, they are compared with reaction rates reported in the REACLIB [76] and STARLIB [77] libraries.

$T$ [GK]	This work	REACLIB	STARLIB
2.0	$3.43 \times 10^{-5}$	$2.38 \times 10^{-5}$	$3.95 \times 10^{-5}$
2.5	$8.11 \times 10^{-5}$	$4.69 \times 10^{-5}$	$9.44 \times 10^{-5}$
3.0	$1.65 \times 10^{-4}$	$8.03 \times 10^{-5}$	$1.93 \times 10^{-4}$
3.5	$2.93 \times 10^{-4}$	$1.23 \times 10^{-4}$	$3.43 \times 10^{-4}$

reactions were calculated for typical  $p$ -process temperatures between 2 and 3.5 GK. As outlined in the introduction, the ratio of these two reactions affects the  $p$ -process path significantly. Table II shows that the  $(\gamma, p)/(\gamma, n)$  ratio obtained from this work is higher than the ratio obtained from the REACLIB [76] library by 40% at  $T = 2.0$  GK. The deviation between our results and the values from the STARLIB library is only about 14%. In addition, the temperature dependence of the  $(\gamma, p)/(\gamma, n)$  ratio differs significantly for both libraries. These results show the impact of the underlying nuclear physics models for the calculation of stellar reaction rates, in particular the nuclear level density and the  $\gamma$ -ray strength function, heavily affect the calculations. Therefore, a detailed understanding and description of those models is of utmost importance.

## V. SUMMARY AND CONCLUSION

In this paper, the experimental cross sections of the  $^{93}\text{Nb}(p, \gamma)^{94}\text{Mo}$  reaction at proton beam energies between 2 and 5 MeV have been investigated. The results yield important information on the reaction path within the  $\gamma$  process in the Mo isotopic chain and exhibit some significant deviations from formerly reported results. We presented an approach that disentangles the effects of NLD and  $\gamma$ -SF, which are crucial parameters that enter the statistical model calculations. The NLD has been fixed to the number of known levels in  $^{94}\text{Mo}$  with respect to the microscopic HFB level-density model from Ref. [48] and is in good agreement with the experimentally obtained level-density data from Oslo-type experiments.

A model-independent hyperparameter optimization approach has been applied to infer  $E1$  and  $M1$  strength func-

tions in  $^{94}\text{Mo}$  that are capable to reproduce the experimental cross sections. A clear enhancement of the  $M1$  decay mode towards lower  $\gamma$ -ray energies has been shown, whereas the  $E1$  functions do not allow us to draw conclusions about a general trend, but seem to be slightly overestimated by the current models above  $E_\gamma \approx 5$  MeV. The sum of  $E1$  and  $M1$ , however, exhibits very little variations and features a low-energy up-bend as well. The overall trend is nicely reproduced by the recently published D1M + QRPA + Olim  $\gamma$ -SF model calculations [70]. This model is an extension of the Gogny D1M + QRPA photoabsorption model to the deexcitation mechanism and includes recent experimental findings with respect to the low-energy limit. We demonstrated that this technique allows us to observe some general trend of strength functions and agrees well with results derived with the Oslo technique. However, the total  $(p, \gamma)$  cross section is not exclusively sensitive to either  $E1$  or  $M1$  strength and, hence, no strength function can be constrained unambiguously. This problem may be overcome by a detailed analysis of primary  $\gamma$ -ray transitions and the corresponding partial cross sections. Since these are extremely sensitive to the spin and parity of the initial state in the excited compound nucleus and to the final (low-lying) state, explicit studies of  $E1$  and  $M1$  will be possible. A forthcoming publication will address these subjects and report on the partial cross-section results. We calculated the  $(\gamma, p)$  and  $(\gamma, n)$  reaction rates on  $^{94}\text{Mo}$  and compared the results to values obtained from the REACLIB and STARLIB libraries. While the discrepancies with respect to the REACLIB library are large, the deviation with respect to the values reported in the STARLIB library are quite small. Hence, we affirm that the underproduction problem of the light  $p$  nuclei in the Mo chain cannot be related to nuclear physics uncertainties. In conclusion, we show that radiative proton-capture reactions not only provide experimental constraints on the reactions rates important for nuclear astrophysics, but can also be used to study the  $\gamma$ -ray strength functions in the compound nucleus.

## ACKNOWLEDGMENTS

We gratefully thank K.O. Zell and A. Blazhev for the target preparation and H.W. Becker and V. Foteinou of the Ruhr-Universität Bochum for the assistance during the RBS measurements. This project has been supported by the Deutsche Forschungsgemeinschaft under the contracts ZI 510/9-1.

- 
- [1] E. M. Burbidge, G. R. Burbidge, W. A. Fowler, and F. Hoyle, *Rev. Mod. Phys.* **29**, 547 (1957).
  - [2] F. Käppeler, R. Gallino, S. Bisterzo, and W. Aoki, *Rev. Mod. Phys.* **83**, 157 (2011).
  - [3] M. Pignatari, R. Gallino, M. Heil, M. Wiescher, F. Käppeler, F. Herwig, and S. Bisterzo, *Astrophys. J.* **710**, 1557 (2010).
  - [4] M. Arnould, S. Goriely, and K. Takahashi, *Phys. Rep.* **450**, 97 (2007).
  - [5] M. Arnould and S. Goriely, *Phys. Rep.* **384**, 1 (2003).
  - [6] T. Rauscher, N. Dauphas, I. Dillmann, C. Fröhlich, Zs. Fülöp, and Gy. Gyürky, *Rep. Prog. Phys.* **76**, 066201 (2013).
  - [7] M. Pignatari, K. Göbel, R. Reifarh, and C. Travaglio, *Int. J. Mod. Phys. E* **25**, 1630003 (2016).
  - [8] S. E. Woosley and W. M. Howard, *Astrophys. J., Suppl. Ser.* **36**, 285 (1978).
  - [9] M. Rayet, M. Arnould, M. Hashimoto, N. Prantzos, and K. Nomoto, *Astron. Astrophys.* **298**, 517 (1995).
  - [10] W. Rapp, J. Görres, M. Wiescher, H. Schatz, and F. Käppeler, *Astrophys. J.* **653**, 474 (2006).
  - [11] C. Fröhlich, G. Martinez-Pinedo, M. Liebendörfer, F.-K. Thielemann, E. Bravo, W. R. Hix, K. Langanke, and N. T. Zinner, *Phys. Rev. Lett.* **96**, 142502 (2006).

- [12] N. Dauphas, T. Rauscher, B. Marty, and L. Reisberg, *Nucl. Phys. A* **719**, C287 (2003).
- [13] C. Travaglio, F. K. Röpke, R. Gallino, and W. Hillebrandt, *Astrophys. J.* **739**, 93 (2011).
- [14] C. Travaglio, R. Gallino, T. Rauscher, F. K. Röpke, and W. Hillebrandt, *Astrophys. J. Lett.* **799**, 54 (2015).
- [15] C. Travaglio, T. Rauscher, A. Heger, M. Pignatari, and C. West, *Astrophys. J. Lett.* **854**, 18 (2018).
- [16] H. Schatz, *J. Phys. G* **43**, 064001 (2016).
- [17] S. Goriely, *Eur. Phys. J. A* **51**, 172 (2015).
- [18] W. Hauser and H. Feshbach, *Phys. Rev.* **87**, 366 (1952).
- [19] T. Rauscher and F.-K. Thielemann, *At. Data Nucl. Data Tables* **75**, 1 (2000).
- [20] T. Rauscher, *Int. J. Mod. Phys. E* **20**, 1071 (2011).
- [21] G. G. Kiss, P. Mohr, Zs. Fülöp, T. Rauscher, Gy. Gyürky, T. Szücs, Z. Halász, E. Somorjai, A. Ornelas, C. Yalçin, R. T. Güray, and N. Özkan, *Phys. Rev. C* **88**, 045804 (2013).
- [22] S. J. Quinn, A. Spyrou, A. Simon *et al.*, *Phys. Rev. C* **92**, 045805 (2015).
- [23] A. Simon, M. Beard, A. Spyrou, S. J. Quinn *et al.*, *Phys. Rev. C* **92**, 025806 (2015).
- [24] L. Netterdon, J. Mayer, P. Scholz, and A. Zilges, *Phys. Rev. C* **91**, 035801 (2015).
- [25] P. Scholz, F. Heim, J. Mayer, C. Münker, L. Netterdon, F. Wombacher, and A. Zilges, *Phys. Lett. B* **761**, 247 (2016).
- [26] T. Szücs, P. Mohr, Gy. Gyürky, Z. Halász, R. Huszánk, G. G. Kiss, T. N. Szegedi, Zs. Török, and Zs. Fülöp, *Phys. Rev. C* **100**, 065803 (2019).
- [27] T. Rauscher, *Phys. Rev. C* **73**, 015804 (2006).
- [28] T. Rauscher, N. Nishimura, R. Hirschi, G. Cescutti, A. St. J. Murphy, and A. Heger, *Mon. Not. R. Astron. Soc.* **463**, 4153 (2016).
- [29] S. Harissopulos *et al.*, *Phys. Rev. C* **64**, 055804 (2001).
- [30] S. Galanopoulos, P. Demetriou, M. Kokkoris, S. Harissopulos, R. Kunz, M. Fey, J. W. Hammer, Gy. Gyürky, Zs. Fülöp, E. Somorjai, and S. Goriely, *Phys. Rev. C* **67**, 015801 (2003).
- [31] A. Sauerwein, J. Endres, L. Netterdon, A. Zilges, V. Foteinou, G. Provas, T. Konstantinopoulos, M. Axiotis, S. F. Ashley, S. Harissopulos, and T. Rauscher, *Phys. Rev. C* **86**, 035802 (2012).
- [32] S. Harissopulos, A. Spyrou, A. Lagoyannis, M. Axiotis, P. Demetriou, J. W. Hammer, R. Kunz, and H.-W. Becker, *Phys. Rev. C* **87**, 025806 (2013).
- [33] J. Mayer, S. Goriely, L. Netterdon, S. Peru, P. Scholz, R. Schwengner, and A. Zilges, *Phys. Rev. C* **93**, 045809 (2016).
- [34] L. Netterdon, A. Endres, S. Goriely, J. Mayer, P. Scholz, M. Spieker, and A. Zilges, *Phys. Lett. B* **744**, 358 (2015).
- [35] F. Heim *et al.*, Nuclear. Instr. Meth. A (unpublished).
- [36] Gy. Gyürky, Zs. Fülöp, F. Käppeler, G. G. Kiss, and A. Wallner, *Eur. Phys. J. A* **55**, 41 (2019).
- [37] A. Koning and D. Rochman, *Nucl. Data Sheets* **113**, 2841 (2012).
- [38] D. Abriola and A. A. Sonzogni, *Nucl. Data Sheets* **107**, 2423 (2006).
- [39] F. Heim, P. Scholz, M. Körschgen, J. Mayer, M. Müller, and A. Zilges, *Phys. Rev. C* **101**, 035805 (2020).
- [40] J. Ziegler, J. Biersack, and M. Ziegler, SRIM - The Stopping and Range of Ions in Matter (2013).
- [41] Huo Junde, Huo Su, and Yang Dong, *Nucl. Data Sheets* **112**, 1513 (2013).
- [42] E. Browne and J. K. Tuli, *Nucl. Data Sheets* **111**, 1093 (2010). 1276.
- [43] F. Bečvář, P. Cejnar, R. E. Chrien, and J. Kopecký, *Phys. Rev. C* **46**, 1276 (1992).
- [44] F. Bečvář *et al.*, *Nucl. Instrum. Methods Phys. Res., Sect. B* **261**, 930 (2007).
- [45] A. Voinov, S. M. Grimes, C. R. Brune, M. Guttormsen, A. C. Larsen, T. N. Massey, A. Schiller, and S. Siem, *Phys. Rev. C* **81**, 024319 (2010).
- [46] M. Wiedeking *et al.*, *Phys. Rev. Lett.* **108**, 162503 (2012).
- [47] P. Scholz *et al.*, *Phys. Rev. C* (to be published).
- [48] S. Hilaire and S. Goriely, *Nucl. Phys. A* **779**, 63 (2006).
- [49] A. Koning and J. Delaroche, *Nucl. Phys. A* **713**, 231 (2003).
- [50] C. H. Johnson, C. C. Trail, and A. Galonsky, *Phys. Rev.* **136**, B1719 (1964).
- [51] T. Rauscher, *Astrophys. J., Suppl. Ser.* **201**, 26 (2012).
- [52] A. Koning, S. Hilaire, and S. Goriely, *Nucl. Phys. A* **810**, 13 (2008).
- [53] W. Dilg, W. Schantl, H. Vonach, and M. Uhl, *Nucl. Phys. A* **217**, 269 (1973).
- [54] A. Gilbert and A. G. W. Cameron, *Can. J. Phys.* **43**, 1446 (1965).
- [55] S. Hilaire, M. Girod, S. Goriely, and A. J. Koning, *Phys. Rev. C* **86**, 064317 (2012).
- [56] R. Chankova *et al.*, *Phys. Rev. C* **73**, 034311 (2006).
- [57] H. Utsunomiya *et al.*, *Phys. Rev. C* **88**, 015805 (2013).
- [58] M. Martini, S. Péru, S. Hilaire, S. Goriely, and F. Lechaftois, *Phys. Rev. C* **94**, 014304 (2016).
- [59] V. Foteinou *et al.*, *Eur. Phys. J. A* **55**, 67 (2019).
- [60] A. Voinov, E. Algin, U. Agvaanluvsan, T. Belgya, R. Chankova, M. Guttormsen, G. E. Mitchell, J. Rekstad, A. Schiller, and S. Siem, *Phys. Rev. Lett.* **93**, 142504 (2004).
- [61] M. Guttormsen *et al.*, *Phys. Rev. C* **71**, 044307 (2005).
- [62] A. C. Larsen *et al.*, *Phys. Rev. Lett.* **111**, 242504 (2013).
- [63] E. Litvinova and N. Belov, *Phys. Rev. C* **88**, 031302(R) (2013).
- [64] A. C. Larsen *et al.*, *J. Phys. G* **44**, 064005 (2017).
- [65] D. Savran, T. Aumann, and A. Zilges, *Prog. Part. Nucl. Phys.* **70**, 210 (2013).
- [66] S. Goriely, *Phys. Lett. B* **436**, 10 (1998).
- [67] A. C. Larsen and S. Goriely, *Phys. Rev. C* **82**, 014318 (2010).
- [68] R. Capote *et al.*, *Nucl. Data Sheets* **110**, 3107 (2009).
- [69] J. Bergstra, D. Yamins, and D. D. Cox, Making a science of model search: Hyperparameter optimization in hundreds of dimensions for vision architectures, in *Proceedings of the 30th International Conference on Machine Learning (ICML)*, 2013 (to be published).
- [70] S. Goriely, S. Hilaire, S. Péru, and K. Sieja, *Phys. Rev. C* **98**, 014327 (2018).
- [71] A. Banu, E. G. Meekins, J. A. Silano, H. J. Karwowski, and S. Goriely, *Phys. Rev. C* **99**, 025802 (2019).
- [72] G. Rusev, R. Schwengner, R. Beyer, M. Erhard, E. Grosse, A. R. Junghans, K. Kosev, C. Nair, K. D. Schilling, A. Wagner, F. Döna, and S. Frauendorf, *Phys. Rev. C* **79**, 061302(R) (2009).
- [73] R. Schwengner, S. Frauendorf, and A. C. Larsen, *Phys. Rev. Lett.* **111**, 232504 (2013).

- [74] B. A. Brown and A. C. Larsen, *Phys. Rev. Lett.* **113**, 252502 (2014).
- [75] R. Schwengner, S. Frauendorf, and B. A. Brown, *Phys. Rev. Lett.* **118**, 092502 (2017).
- [76] R. H. Cyburt, A. M. Amthor, R. Ferguson, Z. Meisel, K. Smith, S. Warren, A. Heger, R. D. Hoffman, T. Rauscher, A. Sakharuk, H. Schatz, F. K. Thielemann, and M. Wiescher, *Astrophys. J., Suppl. Ser.* **189**, 240 (2010).
- [77] A. L. Sallaska, C. Iliadis, A. E. Champagne, S. Goriely, S. Starrfield, and F. X. Timmes, *Astrophys. J., Suppl. Ser.* **207**, 18 (2013).